Sediment Transport in Turbulent Flows with the Lattice Boltzmann Method

Preprint · February 2018

DOI: 10.13140/RG.2.2.18231.62887

2 authors:

Helen Elizabeth Morrison
University of Rostock
4 PUBLICATIONS **8** CITATIONS
SEE PROFILE

Alfred Leder
University of Rostock
124 PUBLICATIONS **2,773** CITATIONS
SEE PROFILE

Sediment Transport in Turbulent Flows with the Lattice Boltzmann Method

Helen E. Morrison[1,*], Alfred Leder

Chair of Fluid Mechanics, University of Rostock, Albert-Einstein-Str. 2, 18059 Rostock, Germany

Abstract

The burial and scour of objects at the bottom of the ocean is governed by a range of different factors and is thus a complex system to simulate with numerical methods. In this work, we present a sediment transport model based on the lattice Boltzmann method which is capable of predicting the influence of a unidirectional flow field on the development of the sand bed in the vicinity of arbitrarily shaped objects, even under turbulent conditions and relatively low resolution. The underlying lattice Boltzmann method for the fluid phase of the simulation is governed by the three-dimensional entropic multi-relaxation time collision model and further makes use of appropriate three-dimensional grid refinement and off-lattice boundaries. The corresponding framework was implemented in the open-source Palabos library and enables accurate turbulent flow simulations around arbitrarily shaped objects without the need to tune any specific model parameters. For the simulation of the sediment transport, the advection-diffusion equation is solved via the lattice Boltzmann method with an adapted version of the entropic multi-relaxation time collision model for a three-dimensional lattice with seven discrete lattice velocities (D3Q7). The presented sediment transport model thus inherits the unconditional numerical stability and the simplicity of the entropic multi-relaxation time collision model. Furthermore, erosion and sedimentation processes are included based on the critical Shields parameter, i.e. on the wall shear stress. An initial simulation of the flow and sediment transport around a horizontally bedded finite cylinder shows that the presented model is generally able to capture the major sediment processes which govern the development of the sand bed.

Keywords: Lattice Boltzmann method, sediment transport, turbulent flows, scour, sedimentation

1. Introduction

The understanding of sediment transport processes in the vicinity of objects is important for a variety of fields. When it comes to designing off-shore wind structures or pipelines for example, the scouring of the objects due to their respective shapes should be minimized as much as possible in order to prevent significant damage to the structures. The shape of the objects usually results in typical sand bed structures which could therefore also be used to characterise objects buried at the bottom of the ocean. An insight into the processes which govern the sediment transport in the vicinity of mines for example is given by Wilkens and Richardson [1].

An important tool towards determining and understanding these processes is numerical simulation. Such simulations under the conditions at the bottom of the ocean or river beds are extremely challenging though, as the flow around the objects is characterised by turbulent structures. These correspondingly affect the erosion and sedimentation of the sand bed, which also needs to be simulated appropriately. In the context of Navier-Stokes solvers, several such numerical models have thus far been introduced in the literature. These very often deal with the sediment transport around vertical cylinders [e.g. 2–5], but also with the sediment transport around horizontally bedded finite cylinders such as mines for example [6] or half-buried spheres [7].

Recently though, the lattice Boltzmann method (LBM) has also become a viable alternative for modelling complex turbulent flows. Beside the fact that no complicated mesh generation is needed and the method exhibits excellent scalability on parallel systems, it is also fairly simple to implement additional physical models [8]. Furthermore, several collision models have recently been introduced which enable numerically stable and accurate turbulent flow simulations without the need of explicit turbulence models [9–13].

Several studies have previously also dealt with simulating sediment transport with the lattice Boltzmann method. Masselot and Chopard [14] and Dupuis and Chopard [15] for example described the transport of snow and sand, respectively, using a combined lattice Boltzmann and cellular automata approach. Parmigiani et al. [16] on the other hand used a large eddy simulation (LES) approach to LBM to simulate the fluid flow and included sediment via an LBM description of the advection-diffusion equa-

*Corresponding author

Email address: helen.morrison@uni-rostock.de (Helen E. Morrison)

[1]Current affiliation: Chair of Ocean Engineering, University of Rostock, Albert-Einstein-Str. 2, 18059 Rostock, Germany

tion. Furthermore, Rettinger et al. [17] combined an LBM fluid simulation with non-smooth granular dynamics to describe the formation of dunes in riverbeds. To the authors knowledge though, no LBM approach to sediment transport has so far been introduced, which is able to couple sediment transport to turbulent flows which rely on collision models that provide unconditional numerical stability. The underlying work aims to provide such an LBM model, which is able to combine the simulation of complex turbulent flows with appropriate sediment transport using the entropic multi-relaxation time lattice Boltzmann model introduced by Karlin et al. [9] and Bösch et al. [10]. One of the main requirements to the model framework is that it should require as few simulation parameters as possible, while providing a good approximation of the resulting flow and sand bed structures. The sediment phase is modelled via an advection-diffusion approach in order to keep the computational cost at a minimum. Furthermore, the framework is required to be able to handle arbitrarily shaped objects and local grid refinement.

2. Fluid Flow Simulations

The following section will provide a detailed outline of the various implementations that were incorporated into the open-source Palabos code [18] for the simulation of the fluid flow. The main intention is to provide a numerical setup that can be used to simulate external flows around arbitrarily shaped with the additional requirement that the simulation remain numerically stable even at high Reynolds numbers. This means that the user should have to provide as few parameters as possible, alongside an STL file of the desired object.

2.1. The Entropic Multi-Relaxation Time Lattice Boltzmann Method

The general form of the lattice Boltzmann equation for incompressible flows is obtained by discretising the Boltzmann equation on a lattice at the grid points $\boldsymbol{x}$ which is spanned by a discrete set of velocity vectors $\boldsymbol{c}_i, i = 0, \ldots, q-1$:

$$f_i(\boldsymbol{x} + \boldsymbol{c}_i, t+1) = f_i(\boldsymbol{x}, t) + \Omega_i, \tag{1}$$

where f_i are distribution functions corresponding to the respective velocity vectors $\boldsymbol{c}_i$ and Ω_i is the collision term. While the left-hand side of the above equation corresponds to a streaming step on the lattice, the right-hand side denotes the post-collision state of the distribution functions.

For the simple case of the single-relaxation time lattice Bathnagar-Gross-Krook (LBGK) model, based on the collision model of Bhatnagar et al. [19], the collision term can be approximated by introducing a local equilibrium $f_i^{\mathrm{eq}}(\boldsymbol{x}, t)$:

$$\Omega_i = -\frac{1}{\tau}\left(f_i(\boldsymbol{x}, t) - f_i^{\mathrm{eq}}(\boldsymbol{x}, t)\right), \tag{2}$$

where the relaxation time τ is related to the kinematic viscosity ν. The equilibrium term itself corresponds to the discretised Maxwell-Boltzmann distribution, which is subsequently expanded up to the second order in $\boldsymbol{u}$:

$$f_i^{\mathrm{eq}} = \rho t_i \left(1 + \frac{\boldsymbol{u}\cdot\boldsymbol{c}_i}{c_s^2} + \frac{(\boldsymbol{u}\cdot\boldsymbol{c}_i)^2 - c_s^2(\boldsymbol{u}\cdot\boldsymbol{u})}{2c_s^4}\right), \tag{3}$$

where $\rho = \sum_i f_i$ is the density, $\boldsymbol{u} = 1/\rho \sum_i \boldsymbol{c}_i f_i$ is the macroscopic velocity, $c_s = 1/\sqrt{3}$ is the sound speed in lattice units and t_i are lattice specific constants. In the hydrodynamic limit, the Navier-Stokes equations are then recovered via the Chapman-Enskog expansion with the kinematic viscosity given by

$$\nu = c_s^2\left(\tau - \frac{1}{2}\right). \tag{4}$$

Unfortunately, the LBGK model rapidly becomes numerically unstable at moderate Reynolds numbers, when $\tau \to 1/2$. Therefore, several collision models have been introduced which aim to increase the stability and accuracy at higher Reynolds numbers. In the following, we will discuss only the entropic multi-relaxation time lattice Boltzmann model, which was introduced by Karlin et al. [9] and is therefore henceforth denoted as the Karlin-Bösch-Chikatamarla (KBC) model. As the name suggests, it can be seen as an extension of both the entropic lattice Boltzmann method (ELBM) [20, 21] and the multi-relaxation time (MRT) lattice Boltzmann models [22–24]: While ELBM makes use of an additional parameter α to locally modify the viscosity in accordance with an entropy condition when and wherever needed, the MRT models make use of the fact that not all moments of the distribution functions need to be relaxed with the same relaxation time in order to obtain the expected hydrodynamic behaviour. The KBC model combines these two aspects in that it keeps the unmodified viscosity and relaxation time for the moments that are relevant for the Navier-Stokes equations, while using an entropy condition to locally fix the relaxation time of the higher order moments.

To begin with, the distribution functions f_i are expressed in the moment basis, where the moments for a three-dimensional lattice with 27 discrete lattice velocities (D3Q27) are given by

$$\rho M_{pqr} = \sum_{i=0}^{26} f_i c_{ix}^p c_{iy}^q c_{iz}^r, \quad p,q,r \in \{0,1,2\},\ c_{i\alpha} \in \{-1,0,1\}. \tag{5}$$

In this basis, the distribution functions can be written as

$$f_i = k_i + s_i + h_i, \tag{6}$$

where k_i is the kinematic part, which depends on the conserved quantities, i.e. the density ρ and the velocity $\boldsymbol{u}$, and s_i denotes the shear part which must at least contain the deviatoric stress tensor. Further moments may also

be included into s_i though, thus yielding a set of various slightly different KBC models. Finally, the contribution of all other higher-order moments is denoted by h_i. Given the expression used in Eq. 6, the collision term becomes

$$\Omega_i = -\frac{1}{\tau}\left[\Delta s_i + \frac{\gamma}{2}\Delta h_i\right] \tag{7}$$

with $\Delta s_i = s_i - s_i^{\mathrm{eq}}$ and $\Delta h_i = h_i - h_i^{\mathrm{eq}}$. This ensures that the kinematic viscosity ν is still given by Eq. 4 while the parameter γ controls the relaxation time of the higher order moments. Following Karlin et al. [9], γ can thus be obtained by maximizing the entropy of the post-collision state under the constraint of a fixed state for the shear stress part. A sufficient approximation to this condition is given by

$$\gamma = 2\tau - 2\left(1-\tau\right)\sum_i \frac{\Delta s_i \Delta h_i}{f_i^{\mathrm{eq}}}\left(\sum_i \frac{\Delta h_i \Delta h_i}{f_i^{\mathrm{eq}}}\right)^{-1}. \tag{8}$$

A more in-depth description of the KBC models can be found in Bösch et al. [10], which also demonstrates the ability of the model to produce accurate results even when the simulation is under-resolved. Further, Dorschner et al. [12] showed that the KBC model - specifically, the model which incorporates only the required deviatoric stress tensor in the shear part s_i - can further be used in the presence of boundaries and is able to produce results comparable to those of direct numerical simulations for both resolved and under-resolved cases. This, together with the fact that no tunable parameters are required in advance, render it the ideal model for the simulation of fluid flows at high Reynolds numbers.

2.2. Off-Lattice Boundary Conditions

Many technical and industrial flow problems involve external flows around complex geometries at high Reynolds numbers (typically up to $Re \approx 10^5 - 10^6$). Because these objects tend to be rather large and their movement is often limited in comparison to the flow, we have chosen an approach based on a modified bounce-back of the distribution function instead of using an immersed boundary method. In order to ensure locality and efficiency of the method, the interpolated bounce-back scheme of Bouzidi, Firdaouss and Lallemand [25] (BFL) was chosen. By separately saving the distribution functions after each collision as $f^C_{i,\mathrm{prev}}$, this bounce-back scheme can be applied locally to the distribution functions which are initially missing after a streaming step:

$$\begin{aligned} f_i^{bb} &= f_{\tilde{i}}(\boldsymbol{x}, t+1)^{C,S} \\ &= \begin{cases} 2\Delta f^C_{i,\mathrm{prev}} + (1-2\Delta) f_i^{C,S} + \dfrac{2t_i}{c_s^2}\left(\boldsymbol{c}_{\tilde{i}} \cdot \boldsymbol{u}_b\right), & \Delta < 1/2 \\ \dfrac{1}{2\Delta} f^C_{i,\mathrm{prev}} + \dfrac{2\Delta - 1}{2\Delta} f^C_{\tilde{i},\mathrm{prev}} + \dfrac{1}{c_s^2 \Delta}\left(\boldsymbol{c}_{\tilde{i}} \cdot \boldsymbol{u}_b\right), & \Delta \geq 1/2 \end{cases} \end{aligned} \tag{9}$$

where $\Delta \in [0,1]$ is the normalized distance of the fluid node to the boundary, $\boldsymbol{u}_b$ is the velocity of the boundary and $\boldsymbol{c}_{\tilde{i}} = -\boldsymbol{c}_i$. Furthermore, $f_i^{C,S}$ denotes the respective distribution functions after both the collide and the streaming step.

Although this approach is extremely efficient and able to reproduce the exact position of the boundary of an object, it can become numerically unstable due to the fact that only a linear interpolation is used. This is especially the case when the considered object is allowed to move and the velocity of the flow becomes increased locally in space and time. The numerical stability can be restored though by applying the Tomm-Mott-Smith (TMS) approximation as proposed by Chikatamarla and Karlin [26] after the interpolated bounce-back step. This combination of both the BFL interpolation and the additional TMS step was previously already introduced in Morrison et al. [27], where it was shown to provide the expected results for the flow around a three-dimensional circular cylinder, while also being able to suppress any potential local discontinuities at the boundaries, thereby rendering it indefinitely numerically stable. Additionally, we also tested the method for several different benchmark cases.

One such case is the two-dimensional flow around a circular cylinder with the diameter D at low Reynolds numbers, $Re = U_\infty D/\nu$, where U_∞ denotes the undisturbed velocity of the flow far away from the cylinder. The flow and thus also the drag force experienced by the cylinder strongly depend on the chosen Reynolds number, making it an ideal test case for off-lattice boundary conditions.

The force acting on the cylinder can be evaluated by using the momentum exchange method [28], which takes the momentum exchange of all boundary nodes $\boldsymbol{x}_b$ into account. By denoting the bounce-backed distribution functions as a sub-set $\bar{D}$, the force can be computed as follows:

$$\boldsymbol{F} = \sum_{(\forall \boldsymbol{x} = \boldsymbol{x}_b)} \sum_{(i \in \bar{D})} f_{\tilde{i}}(\boldsymbol{x}, t)\boldsymbol{c}_{\tilde{i}} - f_i(\boldsymbol{x}, t+1)\boldsymbol{c}_i \tag{10}$$

$$= \sum_{(\forall \boldsymbol{x} = \boldsymbol{x}_b)} \sum_{(i \in \bar{D})} \left[f_{\tilde{i},\mathrm{prev}} + f_i^{bb}\right]\boldsymbol{c}_{\tilde{i}} \tag{11}$$

The drag coefficient per unit length is then given by

$$c_D = \frac{2F_x}{\rho U_\infty^2 D} \tag{12}$$

where F_x is the horizontal force acting on the cylinder. The setup of the simulations was chosen analogously to Dorschner et al. [29], with a minimal resolution of $N = 20$ nodes per D and a lattice velocity of $U_\infty = 0.05$.

The resulting drag forces for Reynolds numbers from $4 \leq Re \leq 300$ are shown in Fig. 1, alongside experimental data from Wieselsberger [30] and Tritton [31] as well as numerical data from Lima E Silva et al. [32] and Shu et al. [33], which both used the immersed boundary method to

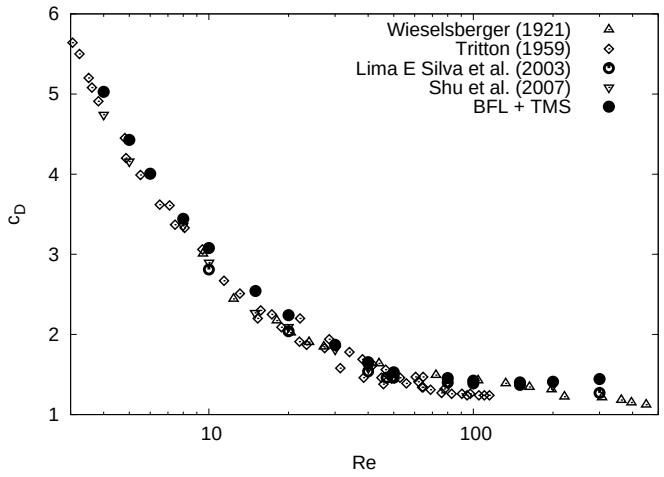

Figure 1: Drag coefficient for the flow around a cylinder at various Reynolds numbers.

accurately depict the geometry of the cylinder. It is apparent that the proposed combination of the BFL interpolation and the subsequent TMS step can accurately reproduce the expected flow behaviour around the cylinder.

Furthermore, the method can also be used to simulate the flow around moving objects. For this, a special treatment is required for solid nodes which become fluid nodes after the object has moved. Several methods for dealing with this have been introduced in the literature, including a second order extrapolation of the distribution functions [34]. For the simulations presented here though, we simply initialize the new fluid cells with the equilibrium distribution function based on the boundary velocity and the average density of the surrounding fluid nodes, which were already fluid nodes during the previous time step.

In order to test the proposed treatment for moving boundaries, we again simulated the flow past a two-dimensional circular cylinder. The simulation domain was chosen to be $L_x = 30D$ long and $L_y = 4D$ wide, with a stationary cylinder placed at $x/D = 2.5$ and $y/D = 2.5$. The inflow velocity in positive x-direction was set to $U_\infty = 0.1$ in lattice units at a Reynolds number of $Re = 200$. The resolution was chosen to be $N = 100$ nodes per D. For comparison, a further simulation was run, where the cylinder was initially placed in a fluid at rest at $x/D = 27.5$ and $y/D = 2.5$ and subsequently moved through the fluid at a velocity of $u_b = -0.1$ in the x-direction. Hence, both simulations depict the same problem but with different frames of reference: once with the cylinder at rest and once with the fluid initially at rest.

Figure 2 shows the resulting vorticity of both runs in comparison at the point where the moving cylinder reaches the same position as the stationary cylinder at $x/D = 2.5$. As expected, both simulations produce an identical flow field, thus proving the capability of the proposed off-lattice boundary condition to accurately depict the flow around (moving) objects.

2.3. Three-dimensional Multi-Domain Grid Refinement

Grid refinement is needed in order to refine certain areas of the simulation to allow for a higher computational accuracy, e.g. directly around the object in order to ensure a correct detachment of the flow. This was achieved by implementing a three-dimensional multi-domain approach to grid refinement, which is essentially a three-dimensional extension of the method outlined in Lagrava et al. [35]. For this approach, the user initially defines a set of boxes within the simulation domain which should be refined. These boxes are then subtracted from the original domain, such that multiple domains of varying resolutions are obtained. The domains then ultimately share an overlapping region of two coarse grid cells, which is used to couple the respective domains.

Following Lagrava et al. [35], the resolution of each refinement domain is twice as high as the resolution of the surrounding domain ($\Delta x_f = \Delta x_c/2$). With the choice of convective scaling, this in turn means that the refinement domain also undergoes twice as many iterations as the surrounding domain ($\Delta t_f = \Delta t_c/2$). Because the Reynolds number must remain the same on both grids, one also obtains a scaling relationship for the respective kinematic viscosities and with Eq. 4 thus also for the relaxation times:

$$\nu_f = 2\nu_c \tag{13}$$

$$\Rightarrow \quad \tau_f = 2\tau_c - \frac{1}{2} \tag{14}$$

The latter is needed to adequately scale the distribution functions between the domains:

$$f_i = f_i^{\mathrm{eq}}(\rho, \boldsymbol{u}) + f_i^{neq}(\rho, \boldsymbol{u}, \boldsymbol{\sigma}) \tag{15}$$

While the equilibrium part only depends on the density and the velocity and is therefore invariant under convective scaling, the non-equilibrium term depends on the deviatoric stress tensor $\boldsymbol{\sigma} \propto \nabla \boldsymbol{u}$ and thus needs to be rescaled accordingly. By considering only those terms of the distribution function that fully recover the Navier-Stokes equations during the Chapman-Enskog expansion, the non-equilibrium term can be approximated as follows:

$$f_i^{\mathrm{neq}} \approx -\frac{\tau t_i \rho}{2c_s^2}\left(c_{i\alpha}c_{i\beta} - c_s^2\delta_{\alpha\beta}\right)\left(\frac{\partial u_\alpha}{\partial x_\beta} + \frac{\partial u_\beta}{\partial x_\alpha}\right) \tag{16}$$

This in turn leads to the following relationship between the respective non-equilibrium parts of the distribution functions:

$$f_{i,f}^{\mathrm{neq}} = \frac{\tau_f}{2\tau_c} f_{i,c}^{\mathrm{neq}} \tag{17}$$

These scaling relations are needed for the coupling between the two domains. When coupling the fine grid to the coarse grid, an additional filtering operation is applied to the non-equilibrium distribution functions in order to

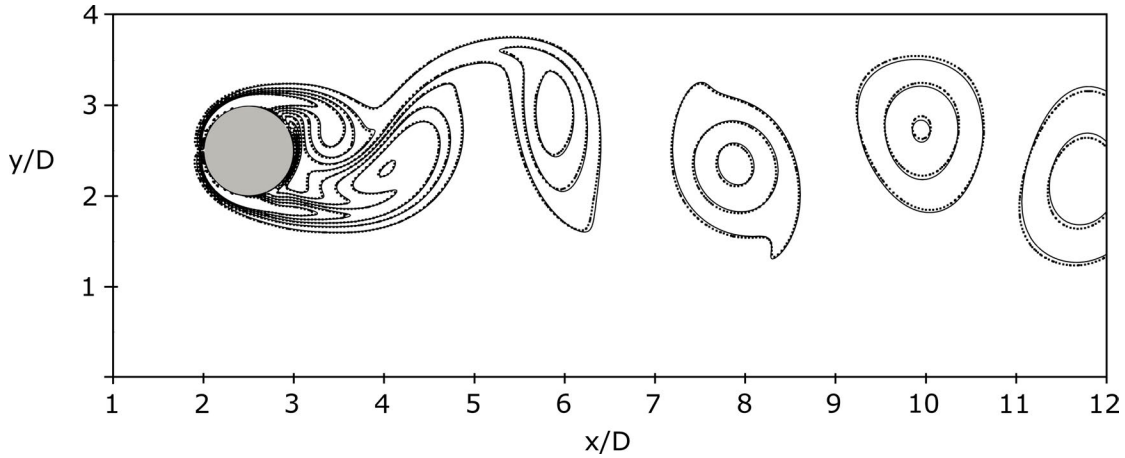

Figure 2: Comparison of the resulting vorticity contours of a moving (dotted lines) and stationary (solid lines) circular cylinder at $Re = 200$, obtained from corresponding LBM simulations using a combined BFL and TMS off-lattice boundary condition.

increase the numerical stability [35]. No such filtering is required though for the coupling from the coarse grid to the fine grid. Nevertheless, for fine grid points that do not coincide with a coarse grid point, the density, the velocity and the non-equilibrium distribution functions need to be interpolated first before the distribution functions can be rescaled. In the three-dimensional case, this interpolation is bi-cubic wherever possible in order to maintain the second order accuracy of the lattice Boltzmann scheme.

2.4. Flow around a Wall-Mounted Finite Cylinder

The aforementioned additions to the open-source Palabos code were combined to simulate the flow around a wall-mounted finite cylinder with an aspect ratio of $L/D = 2$. The flow around such a cylinder has previously been analysed in detail at a Reynolds number of $Re = U_\infty D/\nu = 2 \times 10^5$ within our group, which resulted in a range of measurement data based on three-dimensional laser Doppler anemometry (LDA) [36–38] as well as time-resolved particle image velocimetry (TR-PIV) [39, 40]. Furthermore, this case was also previously simulated using an LES [41–44].

For the simulation of the flow around the wall-mounted cylinder with the lattice Boltzmann method, the cylinder was placed on the floor of the simulation domain at $\boldsymbol{x} = (0, 0, 0)^T$, where T denotes the transpose of the vector for better readability. The domain itself extends over $-1.5 \leq x/D \leq 10.5$, $-5.0 \leq y/D \leq 5.0$ and $0.0 \leq z/D \leq 7.0$ with the flow pointing in the positive x-direction with a velocity of $U_\infty = 0.05$ far away from the influence of the cylinder. The floor is placed at $z/D = 0$. The lateral walls in the y-direction as well as the top wall at $z/D = 7$ are set up as free-slip walls using the specular reflection boundary condition. The outlet at $x/D = 10.5$ is constructed according to the approach outlined in Chikatamarla et al. [45], with an additional sponge zone starting $1D$ before the outlet, where the local viscosity is manually increased in order to dampen the effect of large velocity gradients at the outlet. The inflow velocity corresponds to time-averaged velocity measurements at $x/D = -1.5$ in order to account for the blockage due to the cylinder, though no further temporal variability or artificial turbulence was added.

In order to accurately capture the detachment of the flow, a total of four refinement levels was chosen (Fig. 3). The resolution of the finest refinement box is $N = 80$ nodes per D, resulting in a total of 21.6 million nodes for the entire simulation domain. It is worth pointing out that no specific wall model was used in this case.

Figure 4 shows the contour of the recirculation zone in the mid-plane in the wake of the cylinder, given by the mean horizontal velocity $\bar{u} = 0$. The LBM slightly over-predicts the length of the recirculation zone, which is most likely due to the low resolution close to the ground and the lack of an appropriate wall model. In general though, the shape of the recirculation zone obtained from the lattice Boltzmann simulation agrees well with the TR-PIV measurements [39] and the LES data [42].

Furthermore, Fig. 5 shows the mean velocity and Reynolds stress profiles for a vertical line in the wake of the cylinder in comparison with the previously obtained data from TR-PIV [39] and LDA [38] measurements and from an LES [44]. The profiles obtained from the lattice Boltzmann simulation agree well with the previous data, with the differences between the various simulation techniques being of the same order as the differences between the various experimental data. The obtained profiles thus prove that the LBM is able to accurately capture the flow in the wake of the cylinder.

Overall, the presented simulation shows that the LBM in combination with the KBC model, the aforementioned off-lattice boundaries and multi-domain grid refinement is capable of producing satisfactory results, even at high Reynolds numbers and relatively low resolution.

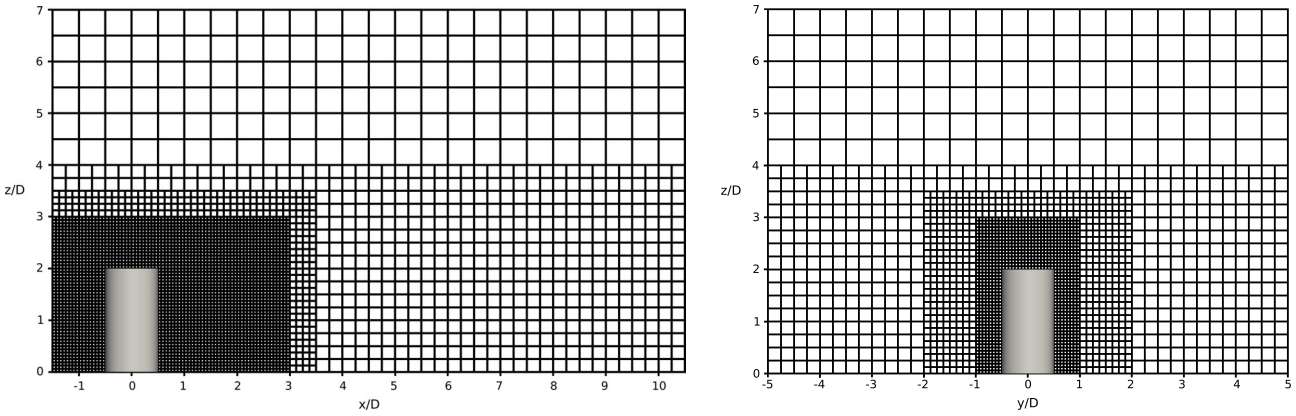

Figure 3: Multi-domain grid comprised of four refinement levels used for the LBM simulation of a wall-mounted cylinder. Every 5th grid node is depicted.

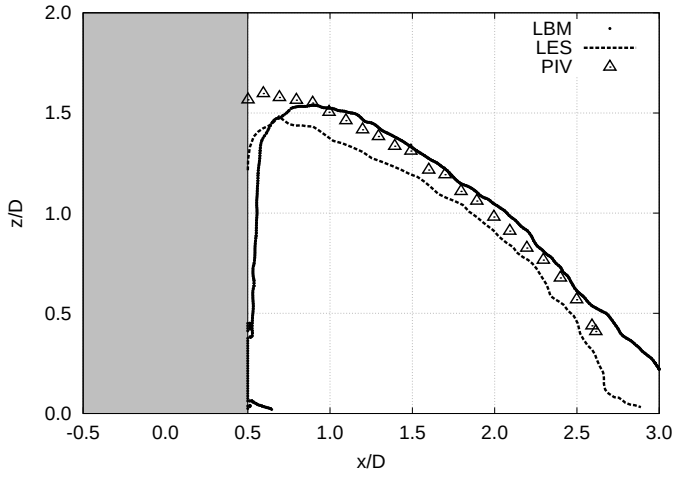

Figure 4: Recirculation zone behind a wall-mounted cylinder at $y/D = 0$. Comparison between averaged LBM, LES and TR-PIV data.

3. Sediment Transport with the Lattice Boltzmann Method

The following section aims to introduce an initial approach to simulating sediment transport around objects in turbulent flows. Because the sediment which is of interest in this study is relatively fine, we shall neglect particle interactions and the effect of the sediment on the fluid. Thus, we will use an advection-diffusion approach to simulate the sediment phase and use a one-way coupling to determine the advection velocity from the fluid simulation.

3.1. The Lattice Boltzmann/Advection-Diffusion Model

The advection and diffusion of an arbitrary quantity φ is given by the following advection-diffusion equation:

$$\frac{\partial}{\partial t}\varphi + \nabla \cdot (\boldsymbol{u}\varphi) = D_0 \nabla^2 \varphi \tag{18}$$

where $\boldsymbol{u}$ denotes the advection velocity and D_0 is the diffusion coefficient. Following Flekkøy [46], it can be shown that the lattice Boltzmann equation (Eq. 1) can also be used to solve the above advection-diffusion equation. In order to distinguish the distribution functions used for the advection-diffusion equation from those used to solve the Navier-Stokes equations, they are usually denoted by g_i in the lattice Boltzmann/advection-diffusion (LB/AD) model:

$$g_i(\boldsymbol{x} + \boldsymbol{c}_i, t+1) - g_i(\boldsymbol{x}, t) = \Omega_i \left(\tau, g_i(\boldsymbol{x}, t), g_i^{\mathrm{eq}}(\boldsymbol{x}, t)\right) \tag{19}$$

The relaxation time τ is then related to the diffusion constant:

$$D_0 = c_s^2 \left(\tau - \frac{1}{2}\right) \tag{20}$$

Furthermore, the advection-diffusion equation does not contain any second-order velocity terms, such that the equilibrium term can be simplified accordingly:

$$g_i^{\mathrm{eq}} = t_i \varphi \left(1 + \frac{1}{c_s^2} \boldsymbol{c}_i \cdot \boldsymbol{u}\right) \tag{21}$$

with $\varphi = \sum_i g_i$. This approach is by far the simplest approach to solving the advection-diffusion equation with the lattice Boltzmann method. Ginzburg [47] further introduced a set of various LB/AD models which also cover special cases, such as anisotropic diffusion, pure advection or pure diffusion. One of these models was used by Stiebler et al. [48] for advection-diffusion problems on non-uniform grids. In their case, no specific scaling of the non-equilibrium part of the distribution function was required when transferring information between the grids. This is indeed required though, when the above LB/AD model is used: for the above case, the non-equilibrium part of the distribution functions, g_i^{neq}, can be approximated by [49]:

$$g_i^{\mathrm{neq}} \approx -\tau t_i \boldsymbol{c}_i \cdot \nabla \varphi \tag{22}$$

This form guarantees that the 0th ($\varphi = \sum_i g_i$) and 1st order moments ($\varphi \boldsymbol{u} = \sum_i \boldsymbol{c}_i g_i$) are dealt with correctly. The equilibrium part of the distribution functions (Eq. 21) only depends linearly on $\boldsymbol{u}$ and therefore remains constant

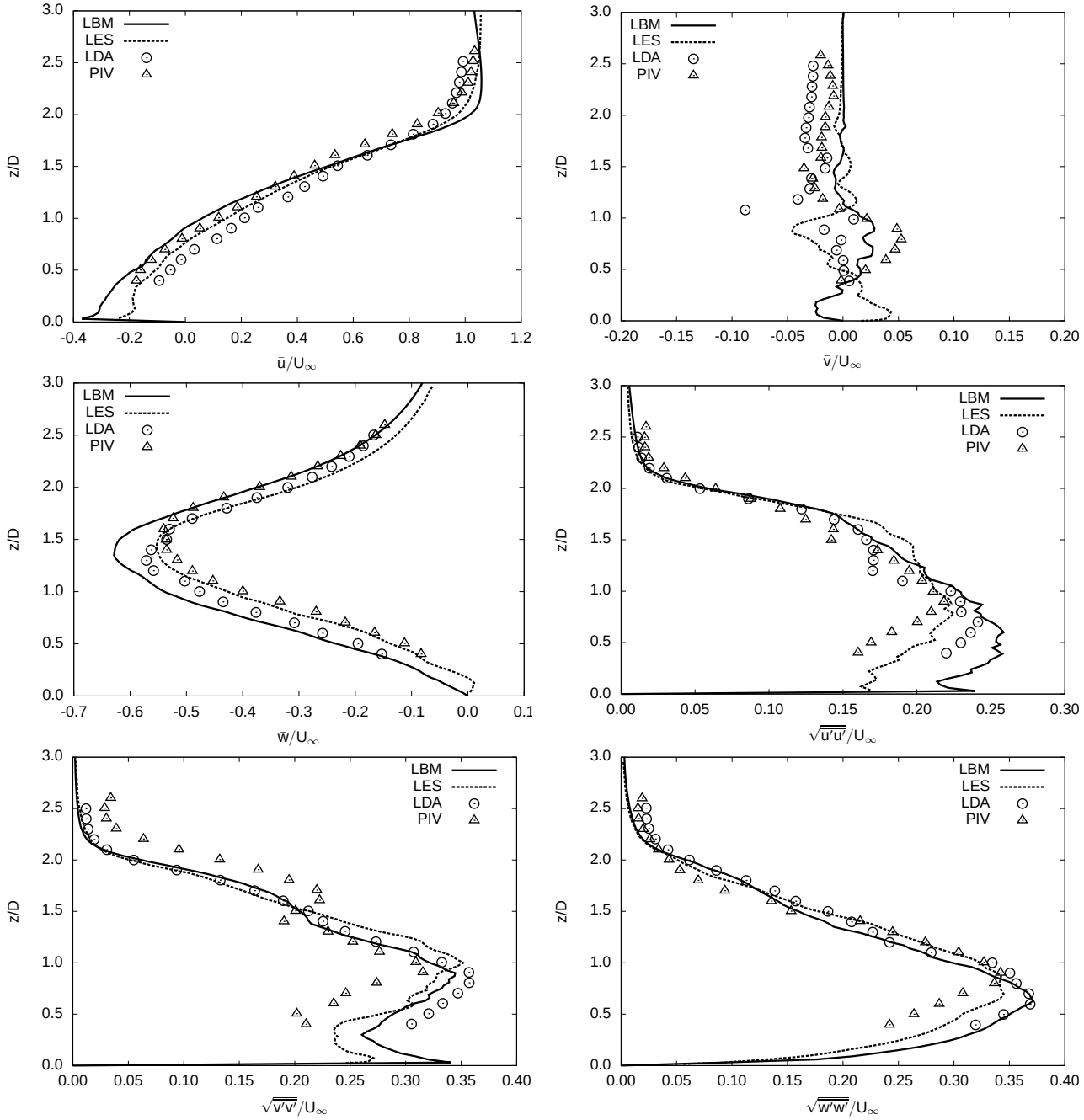

Figure 5: Averaged velocity profiles from the LBM simulation of a wall-mounted cylinder along a vertical line in the wake of the cylinder at $y/D = 0$ and $x/D = 2.2$ in comparison with measurements (TR-PIV and LDA) and LES.

under convective scaling. The non-equilibrium part on the other hand depends on τ and $\nabla\varphi$ and thus needs to be rescaled:

$$g_{i,f}^{\mathrm{neq}} = g_{i,c}^{\mathrm{neq}} \frac{\tau_f (\nabla\varphi)_f}{\tau_c (\nabla\varphi)_c} = g_{i,c}^{\mathrm{neq}} \frac{\tau_f \Delta x_f}{\tau_c \Delta x_c} = g_{i,c}^{\mathrm{neq}} \frac{\tau_f}{2\tau_c} \tag{23}$$

Comparing this to Eq. 17 shows that the scaling of the distribution functions for the LB/AD model is analogous to that of the lattice Boltzmann model used for the fluid flow. This means that no additional treatment is required to adapt the existing multi-domain grid refinement to the LB/AD model.

The LB/AD model can be solved on the D3Q7 lattice. This lattice is defined by the following discretised velocity vectors: $\boldsymbol{c}_0 = (0,0,0)^T$, $\boldsymbol{c}_1 = (1,0,0)^T$, $\boldsymbol{c}_2 = (-1,0,0)^T$, $\boldsymbol{c}_3 = (0,1,0)^T$, $\boldsymbol{c}_4 = (0,-1,0)^T$, $\boldsymbol{c}_5 = (0,0,1)^T$, $\boldsymbol{c}_6 = (0,0,-1)^T$. The lattice constants are given by $t_0 = 1-3c_s^2$ and $t_i = c_s^2/2$ for $i = 1,\ldots,6$. The sound speed is arbitrarily set to $c_s^2 = 1/4$. Because the aim is to eventually combine the LB/AD model with the aforementioned fluid model, a description of the KBC model on the D3Q7 lattice is required. For this we shall first define the moment basis. Following Yoshida and Nagaoka [50] and with

$$M_{pqr} = \sum_{i=0}^{6} g_i c_{ix}^p c_{iy}^q c_{iz}^r, \qquad p,q,r \in 0,1,2 \tag{24}$$

this moment basis is given as follows:

$$\begin{pmatrix} M_{000} \\ M_{100} \\ M_{010} \\ M_{001} \\ 6 - 7(M_{200}+M_{020}+M_{002}) \\ 2M_{200} - M_{020} - M_{002} \\ M_{020} - M_{002} \end{pmatrix} = \begin{pmatrix} 1 & 1 & 1 & 1 & 1 & 1 & 1 \\ 0 & 1 & -1 & 0 & 0 & 0 & 0 \\ 0 & 0 & 0 & 1 & -1 & 0 & 0 \\ 0 & 0 & 0 & 0 & 0 & 1 & -1 \\ 6 & -1 & -1 & -1 & -1 & -1 & -1 \\ 0 & 2 & 2 & -1 & -1 & -1 & -1 \\ 0 & 0 & 0 & 1 & 1 & -1 & -1 \end{pmatrix} \begin{pmatrix} g_0 \\ g_1 \\ g_2 \\ g_3 \\ g_4 \\ g_5 \\ g_6 \end{pmatrix} \tag{25}$$

This in turn results in the following representation of the distribution functions g_i:

$$g_i = \begin{cases} M_{000} - M_{200} - M_{020} - M_{002}, \\ \qquad \text{for } c_{ix} = c_{iy} = c_{iz} = 0 \\ \frac{1}{2}(c_{ix} M_{100} + M_{200}), \\ \qquad \text{for } c_{ix} \neq 0, c_{iy} = c_{iz} = 0 \\ \frac{1}{2}(c_{iy} M_{010} + M_{020}), \\ \qquad \text{for } c_{iy} \neq 0, c_{ix} = c_{iz} = 0 \\ \frac{1}{2}(c_{iz} M_{001} + M_{002}), \\ \qquad \text{for } c_{iz} \neq 0, c_{ix} = c_{iy} = 0 \end{cases} \tag{26}$$

For the KBC model, this representation needs to be split into a part k_i which contains the conserved moments (which in the case of the LB/AD model only includes the 0th order moment), a part s_i which contains all other relevant moments for the model (in this case the 1st order moment) and a part h_i which contains the remaining higher order moments:

$$g_i = k_i(M_{000}) + s_i(M_{100}, M_{010}, M_{001}) + h_i(M_{200}, M_{020}, M_{002}) \tag{27}$$

In order to test this model in combination with multi-domain grid refinement, the advection and diffusion of a Gaussian hill is simulated, which is given by the following distribution:

$$\varphi = \exp\left(-\frac{(\boldsymbol{x} - \boldsymbol{x}_0)^2}{2L}\right) \tag{28}$$

where L is the characteristic length of the domain and $\boldsymbol{x}_0$ is the centre of the distribution. The simulated domain extends over $40L$ in each direction. A refinement box is included between $15 \leq x/L \leq 25$, $20 \leq y/L \leq 30$ and $15 \leq z/L \leq 25$. The resolution of the coarse domain is $N_c = 2$ cells per L and consequently $N_f = 4$. Two Gaussian distributions are defined at an initial position of $\boldsymbol{x}_{0,1} = (15L, 25L, 20L)^T$ and $\boldsymbol{x}_{0,2} = (15L, 15L, 20L)^T$, respectively. The diffusion constant is arbitrarily set to $D_0 = 0.01$ and the advection velocity is chosen to be $\boldsymbol{u} = (U, 0, 0)^T$ with $U = 0.05$, meaning that one Gaussian distribution crosses between the grids, while the other remains on the coarse grid.

Figure 6 shows the temporal evolution of the distributions. Both distributions show the expected behaviour, with no apparent difference between the distribution which crossed between the grids and that which remained on the coarse grid. The presented LB/AD model thus works excellently with both the KBC collision model and the multi-domain grid refinement. Furthermore, it is worth pointing out that no correction term was used. Although Chopard et al. [51] state the necessity of such a term, Flekkøy [46] also pointed out that a correction is not needed if the diffusion constant is low enough, which is in fact the case for all simulations presented in this work.

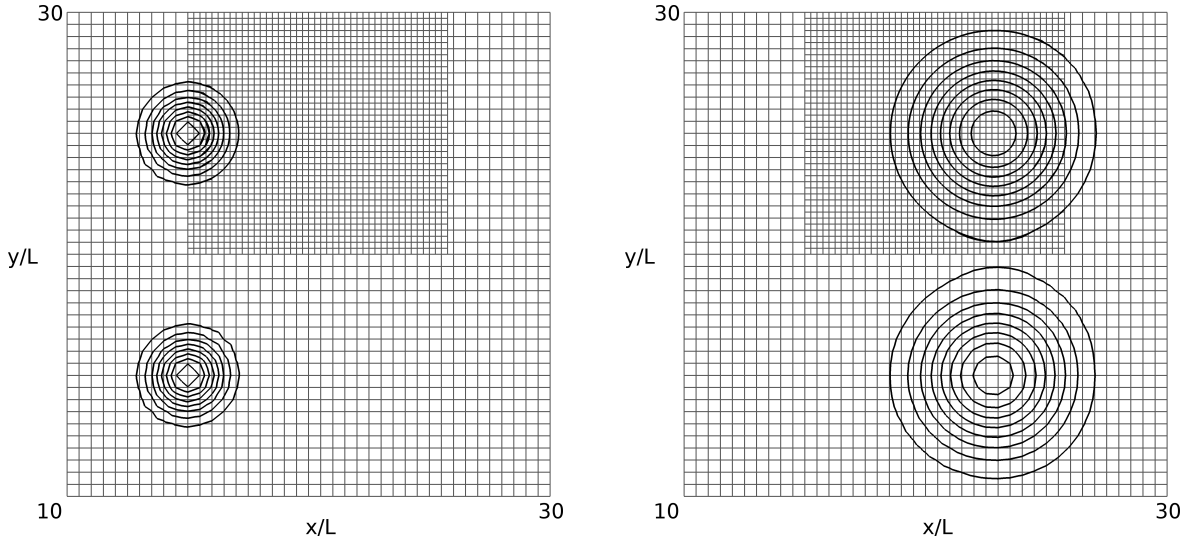

Figure 6: Results from an LBM simulation of the advection and diffusion of two Gaussian hills at $t = 0$ (left) and $t = 147L/U$ (right).

3.2. Coupling the LB/AD Model to the Fluid Flow Simulation

The previously introduced LB/AD model shall now be used to simulate sediment transport in fluid flows around arbitrary objects on a sand bed. In principle, this involves running two simulations side-by-side which are coupled after every iteration step. As already mentioned, only one-way coupling is considered here, where the sediment velocity $\boldsymbol{u}_s$ is determined by the fluid velocity $\boldsymbol{u}$ and an added settling velocity w_s:

$$\boldsymbol{u}_s = \boldsymbol{u} + w_s \boldsymbol{e}_z \tag{29}$$

where $\boldsymbol{e}_z$ is the unit vector in z-direction and it is assumed that gravity acts in the negative z-direction. According to Soulsby [52], The settling velocity is given by

$$w_s = \frac{\nu}{d_s}\left[\sqrt{10.36^2 + 1.049 d_*^3} - 10.36\right] \tag{30}$$

where d_s is the diameter of the considered sediment and d_* is the dimensionless sediment diameter, given by

$$d_* = \left[\frac{(\rho_s - \rho)g}{\rho\nu^2}\right]^{1/3} d_s \tag{31}$$

with the sediment density ρ_s and the gravitational acceleration g. All other parameters are determined by the fluid.

When using the velocity from the fluid flow simulation as the advection velocity though, the previously defined representation for the distribution functions (Eqs. 26 and 27) no longer suffices to achieve numerically stable solutions. Instead, the part s_i, which is most significant for the KBC model (Eq. 7), is defined according to the D3Q27 representation, but using only those moments which are available on the D3Q7 lattice:

$$s_i = \begin{cases} 0, & \text{for } c_{ix} = c_{iy} = c_{iz} = 0 \\ \frac{1}{6}\left(2M_{200} - M_{020} - M_{002}\right), & \text{for } c_{ix} \neq 0, c_{iy} = c_{iz} = 0 \\ \frac{1}{6}\left(2M_{020} - M_{200} - M_{002}\right), & \text{for } c_{iy} \neq 0, c_{ix} = c_{iz} = 0 \\ \frac{1}{6}\left(2M_{002} - M_{200} - M_{020}\right), & \text{for } c_{iz} \neq 0, c_{ix} = c_{iy} = 0 \end{cases} \tag{32}$$

Δs_i in Eq. 7 is thus given by $\Delta s_i = s_i - s_i^{\mathrm{eq}}$ and Δh_i is determined via $\Delta h_i = \Delta f_i - \Delta s_i = f_i - f_i^{\mathrm{eq}} - \Delta s_i$. With this representation, we were able to obtain satisfactory results when using the velocity from the fluid simulation as the advection velocity. The reason behind having to use two different representations, depending on whether a constant advection velocity is used (Eqs. 26 and 27) or velocities from a fluid simulation (Eq. 32), is most likely the fact that the velocities from the fluid flow simulation are themselves part of a simulation based on the KBC model and would thus otherwise cause the sediment simulation to become unstable. Only by applying the same KBC scheme from the fluid simulation to the sediment simulation, it becomes possible to maintain the required numerical stability.

Furthermore, the diffusion constant needs to be determined. This can be obtained via the Schmidt-number $Sc = \nu/D_0$, which couples the viscous diffusion rate of the fluid to the mass diffusivity of the sediment. In the following, this will be set to $Sc = 1$, resulting in the same relaxation parameters for both the fluid and the sediment phase.

3.3. Erosion and Sedimentation

The processes of erosion and sedimentation are handled analogously to Parmigiani et al. [16], where the processes

are effectively controlled via the Shields parameter Sh:

$$Sh = \frac{\tau_w}{(\rho_s - \rho) g d_s} \tag{33}$$

This parameter essentially relates the wall shear stress τ_w to the weight of the sediment. Once the critical Shields parameter Sh_c has been reached, the sediment begins to move and is eroded. The critical Shields parameter itself depends on the considered sediment and can be expressed in terms of the dimensionless sediment diameter [53]:

$$Sh_c = \frac{0.23}{d_*} + 0.054 \left[1 - \exp\left(-\frac{d_*^{0.85}}{23} \right) \right] \tag{34}$$

This, in turn, can be transformed into a critical wall shear stress with Eq. 33. Erosion and sedimentation thus strongly depend on an accurate determination of the wall shear stress, given by the norm of the corresponding vector. Following Stahl et al. [54], this vector can be determined via the deviatoric stress tensor $\boldsymbol{\sigma}$ and the wall normal $\boldsymbol{n}$:

$$\tau_{w,\alpha} = \sigma_{\alpha\beta} n_\beta - (n_\beta \sigma_{\gamma\beta} n_\gamma) n_\alpha \tag{35}$$

Furthermore, $\boldsymbol{\sigma}$ itself can be determined locally and therefore does not require a finite difference method to determine the velocity gradient:

$$\sigma_{\alpha\beta} \approx \left(\frac{1}{2\tau} - 1 \right) \Pi_{\alpha\beta}^{\mathrm{neq}} = \left(\frac{1}{2\tau} - 1 \right) \sum_i c_{i\alpha} c_{i\beta} (f_i - f_i^{\mathrm{eq}}) \tag{36}$$

The wall normal on the other hand also needs to be determined locally, as the erosion and sedimentation processes constantly change the form of the sand bed. For this, a weighted method is chosen, which considers all those velocity vectors that point away from the wall, i.e. away from the sand bed $(\boldsymbol{c}_i, i \in \bar{D})$[55]:

$$\boldsymbol{n} = \frac{1}{\sum_{i \in \bar{D}} w_i} \sum_{i \in \bar{D}} w_i \boldsymbol{c}_i \tag{37}$$

with the weights $w_i = (1 + \Delta_i)^p$ being determined by the respective distances to the wall Δ_i and a weighting factor, which in the following is chosen to be $p = 0.5$.

If the computed wall shear stress in a cell thus exceeds the critical wall shear stress $\tau_{w,c}$, the cell is initially 'marked'. If it remains 'marked' over a given erosion time T_e, i.e. if τ_w remains above $\tau_{w,c}$, then the nearest wall cell along the wall normal is eroded. For the initial simulation, this means that the entire cell becomes a fluid cell which is initialised with $\rho_0 = 1$ and $\boldsymbol{u} = (0, 0, 0)^T$ in the fluid phase and φ_0 in the sediment phase.

Sedimentation on the other hand occurs when $\tau_w \leq \tau_{w,c}$ over a given sedimentation time T_s and the sediment density exceeds a given critical value in the cell $\varphi \geq \varphi_c$. In this case, the respective fluid cell simply becomes a wall cell and no further treatment is required.

In the presented work, the erosion and sedimentation processes are thus fully characterised by the parameters of the erosion time T_e, the sedimentation time T_s and the critical sediment density φ_c. The time scales essentially act as a temporal averaging of the wall shear stresses, but can further be used to control the time scales of the individual processes. For the following, the time scales are arbitrarily set to $T_e = T_s = 10\Delta t_c$, meaning that each individual erosion or sedimentation process requires 10 iterations on the coarse grid. Furthermore, the critical sediment density is arbitrarily set to $\varphi_c = \varphi_0 = 4$.

3.4. Scour and Sedimentation around a Horizontally Bedded Finite Cylinder

The presented models are finally all combined to simulate the sediment processes around a horizontally bedded finite cylinder. Such a cylinder with an aspect ratio of $L/D \approx 3.3$ has previously been a topic of investigation within our group [56], where it was placed on an initially level sand bed in a water channel and subsequently subjected to a uniform flow. The resulting sand structures were then determined qualitatively. Figure 8 shows the sand bed around the cylinder after a quasi-equilibrium state has been reached. Furthermore, Fig. 9 depicts the streamlines from an initial LBM simulation on a flat surface under similar conditions, but without sediment transport. From Fig. 8, it becomes evident that the sand bed upstream of the cylinder has been eroded. This erosion coincides with the formation of a horseshoe vortex that also extends around the edges of the cylinder, as can be made out in Fig. 9. On the other hand, sediment is also deposited downstream of the cylinder, where a recirculation region can be made out from Fig. 9. This suggests that the recirculation region acts as a sediment trap, where the settling velocity cannot be compensated by the fluid flow.

In order to reproduce the sediment transport in this case as well as possible, the simulation parameters were chosen appropriately: the domain extends from $-5 \leq x/D \leq 8$, $-6 \leq y/D \leq 6$ and $-0.2 \leq z/D \leq 2.24$, with the center of the cylinder placed at $x/D = 0$, $y/D = 0$ and $z/D = 0.4$. The chosen refinement boxes are depicted in Fig. 7, with the sand bed completely incorporated in the finest grid. In the experiments, the water surface was approximately $z = 0.13$ m $= 2.24D$ above the sand bed. This surface is not explicitly modelled in the simulation, but approximated by a free-slip boundary condition. Furthermore, the lateral walls are also incorporated as free-slip boundaries, as the actual water channel is slightly wider. At the inlet at $x/D = -5$, a measured average velocity profile is inserted which can be approximated as follows:

$$U = 8.51 U_\infty \left(\frac{z}{D} \right)^{0.35} \tag{38}$$

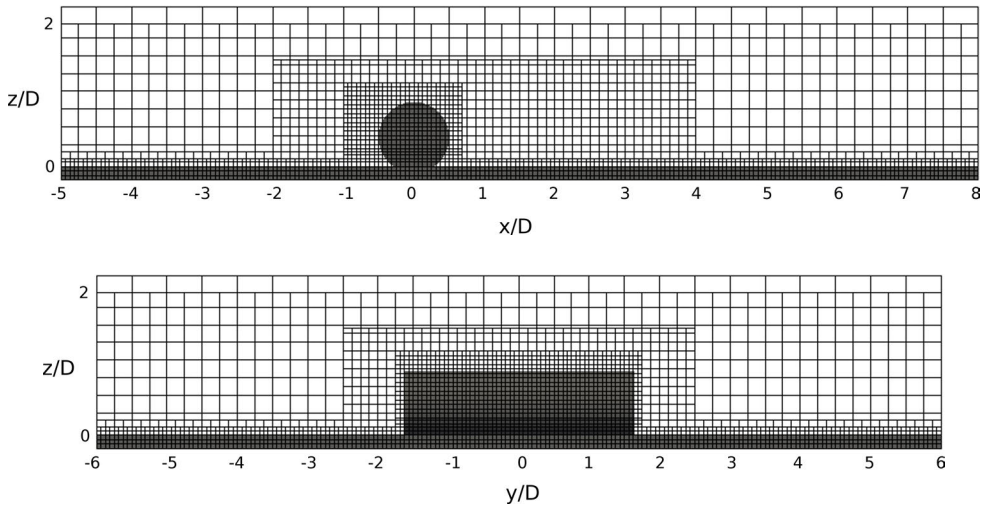

Figure 7: Multi-domain grid comprised of four refinement levels used for the LBM simulation of the flow and sedimentation around a horizontally bedded finite cylinder. Approximately every 5th grid node is depicted.

Figure 8: Photograph of the quasi-equilibrium state of the sand bed around a horizontally bedded finite cylinder in a water channel. The cylinder was subjected to unidirectional flow. The photograph was taken after the sand bed in the direct vicinity of the cylinder no longer exhibited further significant changes.

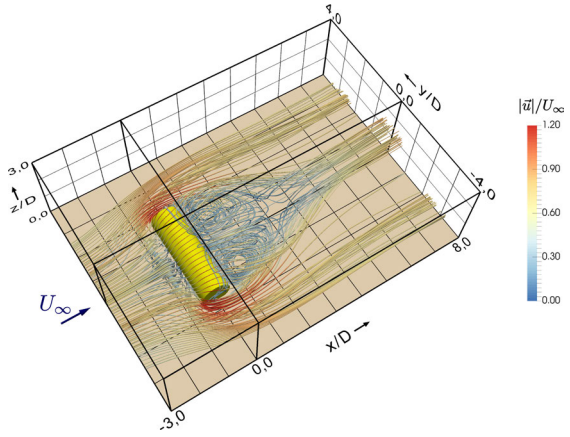

Figure 9: Streamlines from an initial LBM flow simulation around a horizontally bedded finite cylinder.

with $U_\infty = 0.293$ m/s or $U_\infty = 0.05$ in lattice units. The corresponding Reynolds number is $Re = U_\infty D/\nu = 1.7 \times 10^4$. According to the sediment in the water channel, which has a mean sediment diameter of $d_s = 0.2$ mm and a density of $\rho_s = 2600$ kg/m^3, a critical Shields parameter of $Sh_c = 0.054$ was determined, corresponding to a critical wall shear stress of $\tau_{w,c} = 0.17$ N/m^2 or $\tau_{w,c} = 4.97 \times 10^{-6}$ in lattice units.

In order to characterise only the erosion and sedimentation processes due to the cylinder, no initial sediment density was introduced to the sediment phase. This means that the only sediment present in the simulation is that which is eroded from the sand bed. In turn, this also means that the sedimentation processes only become relevant when higher settling velocities are chosen than would be expected from the mean sediment diameter. For the following simulation, the settling velocity is thus chosen to be $w_s = 0.2U_\infty = 5.86$ cm/s, which would normally correspond to a sediment diameter of $d_s \approx 0.4$ mm.

Figure 10 shows the result of the simulation. The fluid flow simulation was given $t = 4000\Delta t_c$ initial runtime before the sediment processes were activated. Evidently, the presented sediment transport model is generally able to capture the main features which determine the sand bed structure around a bedded cylinder: Compared to Fig. 8, the erosion upstream of the cylinder occurs more to the corners and edges of the cylinder, with the area more to the center becoming only gradually eroded during the course of the simulation. It is to be expected that adding avalanching effects to the sediment transport model would gradually cause the sediment directly upstream of the cylinder to fall into the eroded corners, thus increasing the overall eroded area in front of the cylinder. In general though, the overall erosion from the simulation seems to coincide very well with the horseshoe vortex and thus strengthens

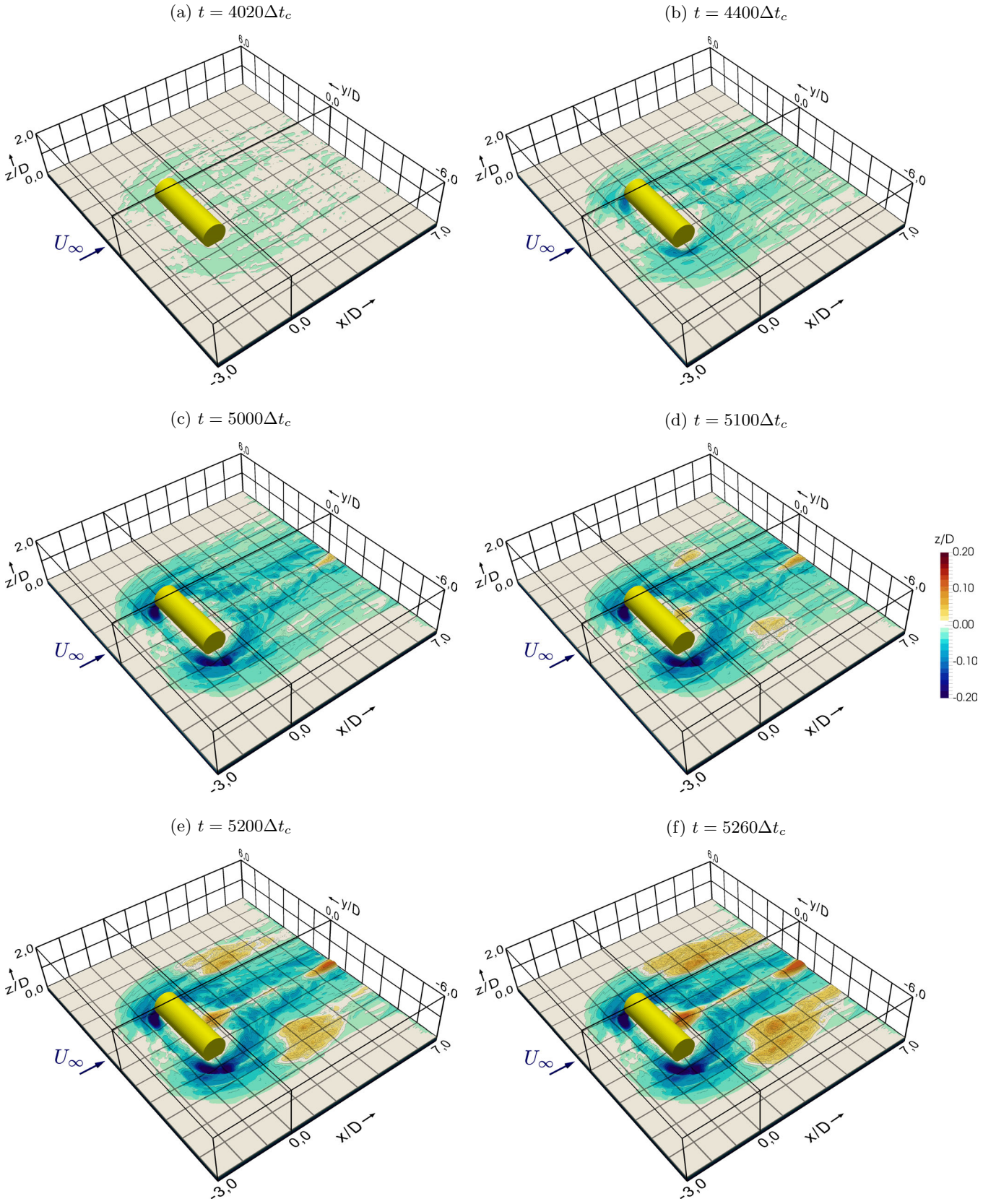

Figure 10: Temporal development of the erosion and sedimentation around a horizontally bedded finite cylinder as obtained from a combined fluid flow and sediment transport simulation using LBM.

the hypothesis that this is the main driving factor behind the scour around the cylinder.
Further, Fig. 10 also shows a gradual deposition of sediment, mainly downstream the center of the cylinder in the recirculation zone. This therefore strengthens the hypothesis that the recirculation zone itself acts as a sediment trap, where the overall velocity of the fluid is not large enough to compensate the settling velocity of the sediment. As the settling velocity increases with the sediment diameter, larger sediment particles are more likely to be deposited in this area, while smaller particles would be transported further downstream.
Additional sedimentation is visible further downstream to the sides of the cylinder. Here, the effect of the cylinder on the fluid flow becomes more and more negligible and the sediment is simply deposited due to its dominant settling velocity.
The simulation was finally cut off after $t = 5260\Delta t_c$, as the eroded sand bed had reached the edge of the simulation domain and the deposited sediment reached the top of the finest grid. Furthermore, the model currently does not account for the fact that the cylinder would at some point begin to roll into the eroded region.

4. Conclusion

The presented work introduced a novel sediment transport model based on the lattice Boltzmann method that can also be used to simulate sediment in complex turbulent flows, even when the simulation is locally under-resolved. The underlying model for the fluid flow simulations relies on the KBC collision model, a combined BFL and TMS approach for off-lattice boundaries and multi-domain grid refinement. This combination has been shown to produce accurate simulation results even at high Reynolds numbers and relatively low resolution. The presented sediment transport model uses an LB/AD model which is based on a modified KBC collision model for the D3Q7 lattice. This therefore enables a direct coupling of the velocity obtained from the fluid flow simulation to the sediment transport simulation. It was also shown though that the KBC model for the D3Q7 lattice needs to be adjusted, depending on whether a constant external advection velocity is used or a local advection velocity which is obtained from a corresponding fluid flow simulation.
An initial simulation of the sediment transport and the resulting sand bed structure in the vicinity of a horizontally bedded finite cylinder showed that the coupling of the aforementioned sediment transport model to turbulent fluid flow simulations delivers the expected results. In order to improve the accuracy of the simulations, several improvements can be included, such as a locally increased resolution of the sand bed, a critical Shields parameter which depends on the inclination of the sand bed, avalanching effects as well as a physically motivated choice of the erosion and sedimentation times T_e and T_s. Furthermore, the presented model can easily be extended to include two-way coupling, e.g. by locally modifying the viscosity of the fluid depending on the local sediment concentration.

Acknowledgements

This work was financed by the International Leibniz Graduate School for Gravity Waves and Turbulence in the Atmosphere and Ocean (ILWAO).

References

[1] R. H. Wilkens, M. D. Richardson, Mine Burial Prediction: A Short History and Introduction, IEEE Journal of Oceanic Engineering 32 (2007) 3–9. doi:10.1109/JOE.2007.894331.

[2] N. R. B. Olsen, H. M. Kjellesvig, Three-dimensional numerical flow modeling for estimation of maximum local scour depth, Journal of Hydraulic Research 36 (1998) 579–590. URL: http://www.tandfonline.com/doi/abs/10.1080/00221689809498610. doi:10.1080/00221689809498610.

[3] M. Zhao, L. Cheng, Z. Zang, Experimental and numerical investigation of local scour around a submerged vertical circular cylinder in steady currents, Coastal Engineering 57 (2010) 709–721. doi:10.1016/j.coastaleng.2010.03.002.

[4] C. Escauriaza, F. Sotiropoulos, Initial stages of erosion and bed form development in a turbulent flow around a cylindrical pier, Journal of Geophysical Research: Earth Surface 116 (2011) 1–24. doi:10.1029/2010JF001749.

[5] H. S. Kim, M. Nabi, I. Kimura, Y. Shimizu, Numerical investigation of local scour at two adjacent cylinders, Advances in Water Resources 70 (2014) 131–147. doi:10.1016/j.advwatres.2014.04.018.

[6] K. A. Hatton, D. L. Foster, P. Traykovski, H. D. Smith, Numerical simulations of the flow and sediment transport regimes surrounding a short cylinder, IEEE Journal of Oceanic Engineering 32 (2007) 249–259. doi:10.1109/JOE.2007.890986.

[7] M. Dixen, B. M. Sumer, J. Fredsøe, Numerical and experimental investigation of flow and scour around a half-buried sphere, Coastal Engineering 73 (2013) 84–105. doi:10.1016/j.coastaleng.2012.10.006.

[8] C. K. Aidun, J. R. Clausen, Lattice-Boltzmann Method for Complex Flows, Annual Review of Fluid Mechanics 42 (2010) 439–472. doi:10.1146/annurev-fluid-121108-145519.

[9] I. V. Karlin, F. Bösch, S. S. Chikatamarla, Gibbs' principle for the lattice-kinetic theory of fluid dynamics, Phys. Rev. E 90 (2014) 031302. doi:10.1103/PhysRevE.90.031302.

[10] F. Bösch, S. S. Chikatamarla, I. V. Karlin, Entropic multirelaxation lattice Boltzmann models for turbulent flows, Phys. Rev. E 92 (2015) 043309. doi:10.1103/PhysRevE.92.043309.

[11] M. Geier, M. Schönherr, A. Pasquali, M. Krafczyk, The cumulant lattice Boltzmann equation in three dimensions: Theory and validation, Computers & Mathematics with Applications 70 (2015) 507–547. doi:10.1016/j.camwa.2015.05.001.

[12] B. Dorschner, F. Bösch, S. Chikatamarla, K. Boulouchos, I. Karlin, Entropic Multi-Relaxation Time Lattice Boltzmann Model for Complex Flows, J. Fluid Mech. 801 (2016) 623–651. doi:10.1017/jfm.2016.448.

[13] M. Geier, A. Pasquali, M. Schönherr, Parametrization of the cumulant lattice Boltzmann method for fourth order accurate diffusion part I: Derivation and validation, Journal of Computational Physics 348 (2017) 862–888. doi:10.1016/j.jcp.2017.05.040.

[14] A. Masselot, B. Chopard, A lattice Boltzmann model for particle transport and deposition, Europhysics letters 42 (1998) 259–264. doi:10.1209/epl/i1998-00239-3.

[15] A. Dupuis, B. Chopard, Lattice Gas Modeling of Scour Formation under Submarine Pipelines, Journal of Computational Physics 178 (2002) 161–174. doi:10.1006/jcph.2002.7025.

[16] A. Parmigiani, J. Latt, M. B. Begacem, B. Chopard, A Lattice Boltzmann simulation of the Rhone river, International Journal of Modern Physics C 24 (2013). doi:10.1142/S0129183113400081.

[17] C. Rettinger, C. Godenschwager, S. Eibl, T. Preclik, T. Schruff, R. Frings, U. Rüde, Fully Resolved Simulations of Dune Formation in Riverbeds, volume 10266 of *High Performance Computing. ISC 2017. Lecture Notes in Computer Science*, Springer, Cham, 2017, pp. 3–21. doi:https://doi.org/10.1007/978-3-319-58667-0_1.

[18] Palabos webpage, 2017. URL: http://www.palabos.org.

[19] P. L. Bhatnagar, E. P. Gross, M. Krook, A Model for Collision Processes in Gases. I. Small Amplitude Processes in Charged and Neutral One-Component Systems, Phys. Rev. 94 (1954) 511–525. doi:10.1103/PhysRev.94.511.

[20] I. V. Karlin, A. Ferrante, H. C. Ottinger, Perfect entropy functions of the Lattice Boltzmann method, Europhys. Lett. 47 (1999) 182–188. doi:10.1209/epl/i1999-00370-1.

[21] S. S. Chikatamarla, S. Ansumali, I. V. Karlin, Entropic lattice Boltzmann models for hydrodynamics in three dimensions, Phys. Rev. Lett. 97 (2006) 1–4. doi:10.1103/PhysRevLett.97.010201.

[22] D. D'Humières, Generalized Lattice-Boltzmann Equations, in: Rarefied Gas Dynamics: Theory and Simulations, volume 159, American Institute of Aeronautics and Astronautics, Washington DC, 1992, pp. 450–458. doi:10.2514/5.9781600866319.0450.0458.

[23] P. Lallemand, L.-S. Luo, Theory of the lattice Boltzmann method: Dispersion, dissipation, isotropy, Galilean invariance, and stability, Physical Review E 61 (2000) 6546–6562. doi:10.1103/PhysRevE.61.6546.

[24] D. D'Humières, I. Ginzburg, M. Krafczyk, P. Lallemand, L.-S. Luo, Multiple-relaxation-time lattice Boltzmann models in three dimensions, Philosophical Transactions of the Royal Society A: Mathematical, Physical and Engineering Sciences 360 (2002) 437–451. doi:10.1098/rsta.2001.0955.

[25] M. Bouzidi, M. Firdaouss, P. Lallemand, Momentum transfer of a Boltzmann-lattice fluid with boundaries, Phys. Fluids 13 (2001) 3452–3459. doi:10.1063/1.1399290.

[26] S. S. Chikatamarla, I. V. Karlin, Entropic lattice Boltzmann method for turbulent flow simulations: Boundary conditions, Physica A 392 (2013) 1925–1930. doi:10.1016/j.physa.2012.12.034.

[27] H. E. Morrison, M. Brede, G. Dehnhardt, A. Leder, Simulating the flow and trail following capabilities of harbour seal vibrissae with the Lattice Boltzmann Method, J. Comput. Sci. (2016). doi:10.1016/j.jocs.2016.04.004.

[28] A. J. C. Ladd, Numerical simulations of particulate suspensions via a discretized Boltzmann equation. Part 1. Theoretical foundation, Journal of Fluid Mechanics 271 (1994) 285–309. doi:10.1017/S0022112094001771.

[29] B. Dorschner, S. Chikatamarla, F. Bösch, I. Karlin, Grad's approximation for moving and stationary walls in entropic lattice Boltzmann simulations, Journal of Computational Physics 295 (2015) 340–354. doi:10.1016/j.jcp.2015.04.017.

[30] C. Wieselsberger, Neuere Feststellungen über die Gesetze des Flüssigkeits- und Luftwiderstandes, Physikalische Zeitschrift 22 (1921) 321–328.

[31] D. J. Tritton, Experiments on the flow past a circular cylinder at low Reynolds numbers, Journal of Fluid Mechanics 6 (1959) 547–567. doi:10.1017/S0022112059000829.

[32] A. Lima E Silva, A. Silveira-Neto, J. Damasceno, Numerical simulation of two-dimensional flows over a circular cylinder using the immersed boundary method, Journal of Computational Physics 189 (2003) 351–370. doi:10.1016/S0021-9991(03)00214-6.

[33] C. Shu, N. Liu, Y. T. Chew, A novel immersed boundary velocity correction-lattice Boltzmann method and its application to simulate flow past a circular cylinder, Journal of Computational Physics 226 (2007) 1607–1622. doi:10.1016/j.jcp.2007.06.002.

[34] P. Lallemand, L.-S. Luo, Lattice Boltzmann method for moving boundaries, Journal of Computational Physics 184 (2003) 406–421. doi:10.1016/S0021-9991(02)00022-0.

[35] D. Lagrava, O. Malaspinas, J. Latt, B. Chopard, Advances in multi-domain lattice Boltzmann grid refinement, J. Comput. Phys. 231 (2012) 4808–4822. doi:10.1016/j.jcp.2012.03.015.

[36] A. Leder, 3D-Flow Structures Behind Truncated Circular Cylinders, in: ASME/JSME 2003 4th Joint Fluids Summer Engineering Conference, Volume 2: Symposia, Parts A, B, and C, ASME, 2003, pp. 825–831. doi:10.1115/FEDSM2003-45083.

[37] F. Richter, A. Leder, Dreidimensionale Strömungs-und Turbulenzstrukturen im Nachlauf eines Kreiszylinderstumpfes., in: Fachtagung Lasermethoden in der Strömungsmesstechnik, Universität Karlsruhe, 2004.

[38] F. Richter, Experimentelle Untersuchungen zur Charakterisierung der Strömungs- und Turbulenzstrukturen im Nachlauf eines Kreiszylinderstumpfes unter Berücksichtigung der Zentrifugalbeschleunigung, Ph.D. thesis, Universität Rostock, 2005.

[39] M. Jensch, M. Brede, F. Richter, A. Leder, Verwendung des Time-Resolved Stereo-PIV Messsystems zur Ermittlung zeitaufgelöster Geschwindigkeitsfelder im Nachlauf eines Kreiszylinders, in: Lasermethoden in der Strömungsmesstechnik - 14. Fachtagung der GALA e.V., PTB Braunschweig, 2006, pp. 39.1–39.8.

[40] M. Jensch, F. Hüttmann, M. Brede, A. Leder, Optical measurements in the wake of a circular cylinder of finite length at a high reynoldsnumber, Notes on Numerical Fluid Mechanics and Multidisciplinary Design 106 (2009) 185–195. doi:10.1007/978-3-642-01106-1_19.

[41] O. Frederich, E. Wassen, F. Thiele, M. Jensch, M. Brede, F. Hüttmann, A. Leder, Numerical Simulation of the Flow Around a Finite Cylinder with Ground Plate in Comparison to Experimental Measurements, in: New Results in Numerical and Experimental Fluid Mechanics VI, volume 96, Springer Berlin Heidelberg, Berlin, Heidelberg, 2007, pp. 348–355. doi:10.1007/978-3-540-74460-3_43.

[42] O. Frederich, E. Wassen, F. Thiele, Prediction of the flow around a short wall-mounted finite cylinder using LES and DES, Journal of Numerical Analysis, Industrial and Applied Mathematics 3 (2008) 231–247.

[43] O. Frederich, J. Scouten, D. M. Luchtenburg, F. Thiele, Numerical Simulation and Analysis of the Flow Around a Wall-Mounted Finite Cylinder, in: Imaging Measurement Methods for Flow Analysis, volume 106, 2009, pp. 207–216. doi:10.1007/978-3-642-01106-1_21.

[44] O. Frederich, Numerische Simulation und Analyse turbulenter Strömungen am Beispiel der Umströmung eines Zylinderstumpfes mit Endscheibe, Ph.D. thesis, Technische Universität Berlin, 2010.

[45] S. S. Chikatamarla, S. Ansumali, I. V. Karlin, Grad's approximation for missing data in lattice Boltzmann simulations, Europhysics Letters 74 (2006) 215–221. doi:10.1209/epl/i2005-10535-x.

[46] E. G. Flekkøy, Lattice Bhatnagar-Gross-Krook models for miscible fluids, Physical Review E 47 (1993) 4247–4257. doi:10.1103/PhysRevE.47.4247.

[47] I. Ginzburg, Equilibrium-type and link-type lattice Boltzmann models for generic advection and anisotropic-dispersion equation, Advances in Water Resources 28 (2005) 1171–1195. doi:10.1016/j.advwatres.2005.03.004.

[48] M. Stiebler, J. Tölke, M. Krafczyk, Advection-diffusion lattice Boltzmann scheme for hierarchical grids, Computers and Mathematics with Applications 55 (2008) 1576–1584. doi:10.1016/j.camwa.2007.08.024.

[49] J. Lätt, Hydrodynamic limit of lattice Boltzmann equations, Dissertation, Univ. Genève, 2007. URL: http://archive-ouverte.unige.ch/unige:464.

[50] H. Yoshida, M. Nagaoka, Multiple-relaxation-time lattice Boltzmann model for the convection and anisotropic diffusion equation, Journal of Computational Physics 229 (2010) 7774–7795. doi:10.1016/j.jcp.2010.06.037.

[51] B. Chopard, J. L. Falcone, J. Latt, The lattice Boltzmann advection-diffusion model revisited, European Physical Journal: Special Topics 171 (2009) 245–249. doi:10.1140/epjst/e2009-01035-5.

[52] R. Soulsby, Dynamics of Marine Sands, Thomas Telford Ltd, 1997. doi:10.1680/doms.25844.

[53] J. Guo, Hunter rouse and shields diagram, Advances in Hydraulic and Water Engineering 2 (2002) 1096–1098. doi:10.1142/9789812776969_0200.

[54] B. Stahl, B. Chopard, J. Latt, Measurements of wall shear stress with the lattice Boltzmann method and staircase approximation of boundaries, Computers and Fluids 39 (2010) 1625–1633. doi:10.1016/j.compfluid.2010.05.015.

[55] M. Matyka, Z. Koza, Ł. Mirosław, Wall orientation and shear stress in the lattice Boltzmann model, Computers and Fluids 73 (2013) 115–123. doi:10.1016/j.compfluid.2012.12.018. arXiv:1203.3078.

[56] P. Menzel, T. Rückborn, A. Leder, Flow and Scour around Cylindrical Objects in Laboratory Experiments., in: Proceedings of 2013 MTS / IEEE Oceans-Bergen IEEE Catalog-Nr.: CFP130CF-CDR 2013, 2013.